

Article

Simulation Analysis on the Optimal Imaging Detection Wavelength of SO₂ Concentration in Ship Exhaust

Zhenduo Zhang, Wenbo Zheng, Kai Cao, Ying Li * and Ming Xie 

Navigation College, Dalian Maritime University, Dalian 116026, China; zhangzhenduo@dmlu.edu.cn (Z.Z.); zwb123456789@dmlu.edu.cn (W.Z.); caokai@dmlu.edu.cn (K.C.); mingxie@dmlu.edu.cn (M.X.)

* Correspondence: yldmu@dmlu.edu.cn

Received: 25 September 2020; Accepted: 18 October 2020; Published: 19 October 2020



Abstract: The SO₂ discharged by ships causes serious pollution to the atmosphere. Therefore, the International Maritime Organization has set strict requirements on the sulfur content of marine fuel. For the first time, this study investigates the optimal detection wavelength based on the imaging technology to realize an accurate monitoring of the SO₂ concentration in ship exhaust. First, a simulation analysis model of the optimal imaging detection (SAMID) wavelength of the SO₂ concentration in ship exhaust is proposed and analyzed in this study. Next, a bench experiment is designed. The values and the range of the gas concentration values required for the simulation are obtained. Finally, based on the principle of minimum error, the optimal detection wavelengths of the single- and the dual-wavelength imaging detection technologies are determined as 287 nm and 297 nm and 298 nm, respectively. During the SO₂ concentration retrieval, the minimum values of the root mean squared error, the mean absolute error, and the mean absolute percentage error of the single- and the dual-wavelengths are 563.14 molecules/cm³, 445.11 molecules/cm³, and 347.22% and 0.62 molecules/cm³, 0.49 molecules/cm³, and 0.85%, respectively. The simulation analysis results provide a theoretical basis for the future hardware development of an optical remote sensing system based on the imaging detection technology.

Keywords: ship emissions; exhaust plume; SO₂ concentration; simulation analysis; imaging detection

1. Introduction

Since the beginning of the 20th century, the impact of ship emissions on the atmosphere has continued to increase as coal-fired ships started to replace sailing vessels. Ship emissions mainly include carbon dioxide (CO₂), carbon monoxide (CO), nitrogen oxide (NO_x), sulfur dioxide (SO₂), methane (CH₄), black carbon (BC), and organic carbon (OC) [1]. As a poisonous gas, SO₂ produces acid rain when it meets with rain in the atmosphere. This not only hugely affects the air and the ecological environment but also damages human health. To effectively control the SO₂ concentration discharged by ships, the International Maritime Organization promulgated and implemented the International Convention for the Prevention of Pollution from Ships (MARPOL). MARPOL requires that the sulfur content of marine fuel in emission control areas (ECAs) should not exceed 0.1% (m/m) by 2015, while that of global marine fuel should contain no more than 0.5% (m/m) by 2020 [2]. Initially, law enforcement personnel mainly adopted the supervision method of sampling and inspection on board to detect the sulfur content of berthing ships and effectively monitor and control marine fuel quality. However, this approach is time consuming and laborious and cannot realize supervision of ships in the sea. At present, the methods of measuring the SO₂ concentration in ship exhaust and calculating the sulfur content of fuel according to the SO₂ concentration are gradually being adopted

internationally for supervision [3–6]. Therefore, the detection accuracy of the SO₂ concentration directly affects the calculation accuracy of the sulfur content as well as the supervision ability and the law enforcement efficiency of regulatory authorities.

In the aspect of SO₂ concentration monitoring, the sniffer technology is currently widely used in Europe and America to supervise vessels in ECAs [7]. Sniffer instruments can be installed in airborne and shipborne platforms, bridges, and ports using the contact exhaust detection method. However, the detection efficiency of the sniffer technology is low, and the distant target detection accuracy is low, which limits the wide application of the sniffer technology. With the development of the optical detection technology, optical remote sensing detection is being gradually applied in ship exhaust monitoring and mainly includes the laser radar technique (LIDAR), differential optical absorption spectroscopy (DOAS), and imaging detection technology [8]. LIDAR is an active detection method. Single LIDAR detection belongs to point target detection, which requires scanning to determine the SO₂ distribution. Moreover, the LIDAR system is complex, has high maintenance cost, and requires large equipment; hence, it is inconvenient to carry, and its echo is easily affected by the atmosphere to produce meandering, which reduces the detection accuracy [9]. Similarly, single DOAS detection belongs to point target detection; thus, the SO₂ concentration within the entire ship exhaust range must be obtained by scanning. Each detection in the scanning process requires a certain amount of time to obtain the broadband absorption spectrum of SO₂; hence, the temporal resolution of DOAS is limited [10]. Meanwhile, the imaging detection technology uses the two-dimensional imaging information of images to invert the SO₂ concentration. It is cheap, easy to carry, and has high temporal and spatial resolutions. It can also obtain “plume” wind speed and gas flux by analyzing the image features. Merico et al. [11] directly measured the flow-rate-emission (FRE) of NO₂ and SO₂ of ships in the harbor area using UV-Vis remote sensing DOAS system, which included a rotating platform called scanning optical device collecting atmospheric light (SODCAL) and a spectrometer. The emission inventory estimation of NO₂ and SO₂ emissions agreed with those measured by DOAS, which indicated that the remote sensing technique could be employed to monitor gaseous emissions from ships. For the first time, Prata [12] applied the single-wavelength imaging detection technology to detect the SO₂ concentration and the emission rate in the plumes of sailing and berthing ships. The single-wavelength position was set at 310 nm. The detection results showed that the accuracy of the single-wavelength imaging detection technology is limited, while the dual-wavelength detection system for detecting ship exhaust must be further developed. Volten et al. [13–16] applied the dual-wavelength imaging detection technology to study volcanology. They determined the dual-wavelength positions at 310 nm and 330 nm.

Our research team intends to use the imaging detection technology to obtain the SO₂ concentration in ship exhaust. The 310 nm and the 330 nm positions used for the volcano detection are not the best wavelength positions for the ship exhaust detection because of the difference in the composition and the proportion of volcanic gases and ship exhaust. However, up to date, no literature has focused on modeling and studying the optimal detection wavelength position of the SO₂ concentration imaging detection technology in ship exhaust.

The optimal wavelength position of the imaging detection technology was analyzed in this study to accurately measure the SO₂ concentration.

The remainder of this paper is structured as follows: Section 2 introduces the simulation analysis model of the optimal imaging detection wavelength of the SO₂ concentration in ship exhaust; Section 3 presents the designed bench experiment for obtaining the value and the range of the gas concentration required for the simulation; and Section 4 discusses bench experiment results as well as the optimal wavelength position and the sulfur content calculation error analysis results of the single- and the dual-wavelengths. The error sources are also discussed, providing a theoretical basis for future hardware development based on the imaging detection technology and the accurate inversion of the SO₂ concentration.

2. Methodology

2.1. Simulation Scheme

2.1.1. Simulation Analysis Model

The law of light absorption, which is also known as the Lambert–Beer law, is the theory of the quantitative analysis of the absorption effect of all light-absorbing substances, including molecules, atoms, ions, solids, liquids, and gases, on all electromagnetic radiation spectra. The law of light absorption is expressed as follows:

$$I(\lambda) = I_0(\lambda) \exp \left[-L(c_{\text{SO}_2} \sigma_{\text{SO}_2}(\lambda) + \sum_{i=1}^n \sigma_i(\lambda) c_i) \right] \quad (1)$$

where I_0 is the initial light intensity; I is the light intensity received by the optical system after extinction of the absorbing gas; L is the optical path length; λ is the light source spectrum wavelength; c_{SO_2} is the SO_2 concentration; $\sigma_{\text{SO}_2}(\lambda)$ is the SO_2 absorption cross-section corresponding to the wavelength; c_i is the concentration of the other absorbing gases, except SO_2 ; $\sigma_i(\lambda)$ is the absorption cross-section of the other absorbing gases; and n is the number of the other types of absorbing gases. $\ln[I_0(\lambda)/I(\lambda)]$ is denoted by $D(\lambda)$, which defines the optical thickness of the absorbed gas. According to Equation (1), the formula for calculating the SO_2 concentration with a single wavelength can be expressed as follows after ignoring the scattering and other gas absorption effects:

$$c_{\text{SO}_2} = D(\lambda) / (L \sigma_{\text{SO}_2}(\lambda)) \quad (2)$$

Equation (3) is obtained as follows after adding the modification of the extinction effect of BC in Equation (1):

$$I(\lambda) = I_0(\lambda) \exp \left[-L(c_{\text{SO}_2} \sigma_{\text{SO}_2}(\lambda) + \sum_{i=1}^n \sigma_i(\lambda) c_i) + D_{\text{BC}}(\lambda) \right] \quad (3)$$

According to Equation (3):

$$D(\lambda) = L(c_{\text{SO}_2} \sigma_{\text{SO}_2}(\lambda) + \sum_{i=1}^n \sigma_i(\lambda) c_i) + D_{\text{BC}}(\lambda) \quad (4)$$

The optical thickness of BC is calculated as follows by Equation (5) when the wavelength is λ [12]:

$$D_{\text{BC}}(\lambda) = m_{\text{bc}} \times k_{\text{bc}}(\lambda) \quad (5)$$

where m_{bc} is the mass concentration of BC (g/m^2), and $k_{\text{bc}}(\lambda)$ is its mass absorption coefficient. Buffalo et al. [17] suggested that the mass absorption coefficient of BC could be calculated as follows:

$$k_{\text{bc}}(\lambda) = k_{\text{bc}}(550) \times (550/\lambda) \quad (6)$$

where $k_{\text{bc}}(550) = 7.5 \pm 1.5 \text{ m}^2/\text{g}$. In this paper, we take $k_{\text{bc}}(550) = 7.5 \text{ m}^2/\text{g}$.

The optical thickness at λ_1 and λ_2 can be expressed as follows according to Equations (4) and (5):

$$D(\lambda_1) = L(c_{\text{SO}_2} \sigma_{\text{SO}_2}(\lambda_1) + \sum_{i=1}^n \sigma_i(\lambda_1) c_i) + m_{\text{bc}} \times k_{\text{bc}}(\lambda_1) \quad (7)$$

$$D(\lambda_2) = L(c_{\text{SO}_2} \sigma_{\text{SO}_2}(\lambda_2) + \sum_{i=1}^n \sigma_i(\lambda_2) c_i) + m_{\text{bc}} \times k_{\text{bc}}(\lambda_2) \quad (8)$$

Assume that NO₂ and BC extinction does not change with the wavelength change:

$$\sum_{i=1}^n \sigma_i(\lambda_1) c_i \approx \sum_{i=1}^n \sigma_i(\lambda_2) c_i \quad (9)$$

$$m_{bc} \times k_{bc}(\lambda_1) \approx m_{bc} \times k_{bc}(\lambda_2) \quad (10)$$

Equations (7) and (8) results in Equation (11):

$$D(\lambda_1) - D(\lambda_2) = L(\sigma_{so_2}(\lambda_1) c_{so_2} - \sigma_{so_2}(\lambda_2) c_{so_2}) \quad (11)$$

According to Equation (11), the dual-wavelength SO₂ concentration calculation formula can be expressed as follows:

$$c_{so_2} = (D(\lambda_1) - D(\lambda_2)) / (L \times (\sigma_{so_2}(\lambda_1) - \sigma_{so_2}(\lambda_2))) \quad (12)$$

After the SO₂ concentration was obtained, three error indicators, namely root mean square error (RMSE), mean absolute error (MAE), and mean absolute percentage error (MAPE), were used to evaluate the accuracy of the SO₂ concentration calculation. The optimal detection wavelength was selected according to the principle of minimum error. The calculation methods of the three error indicators are presented below:

$$MAE = \frac{1}{k} \sum_{i=1}^k |c_{true} - c_{forecast}| \quad (13)$$

$$RMSE = \sqrt{\frac{1}{k} \sum_{i=1}^k |c_{true} - c_{forecast}|^2} \quad (14)$$

$$MAPE = \frac{1}{k} \sum_{i=1}^k \left| \frac{c_{true} - c_{forecast}}{c_{true}} \right| \times 100\% \quad (15)$$

where c_{true} is the true SO₂ concentration; $c_{forecast}$ is the SO₂ concentration calculated by the model; and k is the number of the groups of collected concentration data. As a short summary, the simulation analysis model of the optimal imaging detection (SAMID) wavelength of the SO₂ concentration in ship exhaust is established in this study as above.

2.1.2. Simulation Parameter Selection

On the basis of the established theoretical model, we needed to determine the parameter value according to the actual situation of the ship emission. The imaging detection technology was used herein to detect the tail gas discharged from the chimney. We assumed that, when the tail gas was discharged from the chimney, SO₂ and BC concentrations remained unchanged. We also assumed that the optical path L was approximately equal to the chimney diameter. Therefore, the optical path L was 0.8 m. As for the wavelength range selection, almost all of the UV light less than 280 nm was absorbed by O₃ in the atmosphere [18]; hence, we did not consider the wavelength less than 280 nm. We only selected the integer wavelengths between 280 and 380 nm, where SO₂ had an obvious absorption structure. Most NO_x exists in the form of NO when the exhaust from ships is not in contact with air; thus, the NO concentration is detected in the flue. NO is rapidly transformed into NO₂ [19] after it reacts with O₃ in the air. Beecken et al. [7] showed that 15–50% of the NO_x emitted by ships is transformed into NO₂, and the specific value depends on the distance of the tail gas emission. For the tail gas discharged from the chimney, we assumed that 15% of NO was converted into NO₂. For the unit conversion of concentration quantified as vertical column density, 1 ppm = 2.5×10^{15} molecules/cm² under the conditions of a standard atmospheric pressure and

20 °C were assumed in the whole paper [20]. Figure 1 illustrates the absorption cross-sections of SO₂ and NO₂ at room temperature [21]. We performed linear interpolation on the absorption cross-section data to obtain the absorption cross-section data corresponding to the integer wavelengths in the 280–380 nm range. In our dual-wavelength simulation analysis, the extinction coefficients of NO₂ and BC significantly increased with the increase of wavelength interval. However, in the dual-wavelength inversion of SO₂ concentration, the extinction coefficients of NO₂ and BC at two different wavelengths were considered as the same value. Therefore, a small wavelength interval (e.g., 1–30 nm) is favorable in order to reduce the error introduced from the extraction coefficients of NO₂ and BC and thus achieve accurate inversion results.

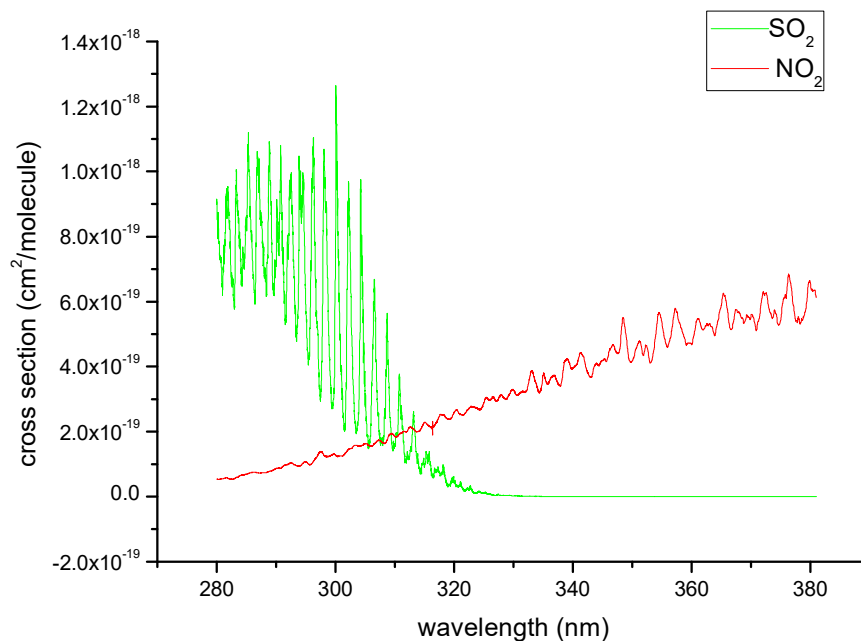


Figure 1. SO₂ absorption cross-section and NO₂ absorption cross-section (data source: The HITRAN 2016 molecular spectroscopic database [21]).

The SAMID model was used for the simulation analysis after the parameter determination. In the single-wavelength simulation analysis, all integer wavelengths between 280 nm and 380 nm were traversed to obtain the single-wavelength simulation analysis data. Meanwhile, in the dual-wavelength simulation analysis, all integer wavelengths between 280 nm and 380 nm and all the integer wavelength intervals between 1 nm and 30 nm were traversed to obtain the dual-wavelength simulation analysis data.

2.2. Experimental Design

A bench experiment was performed to obtain the ship emission data closest to the actual situation used to determine the optimal detection wavelength position of the imaging detection technology. Six kinds of fuel with a sulfur content ranging from 0.1 to 2.0% and 13 kinds of stable conditions ranging from 0 to 100% were used for this experiment. An online monitoring equipment was used to collect the gas concentration data by punching a hole on the flue.

2.2.1. Experimental Diesel Engine

The MAN B&W 6S35ME-B9 diesel engine (Figure 2) was the main engine used in the bench experiment. The main engine is an electronically controlled two-stroke six-cylinder cross-head-type ship main engine with 3400 kW power, 142 r/min rated speed, 3.5% allowable maximum marine fuel sulfur content, and 30,000 kg/h approved maximum tail gas handling capacity.



Figure 2. Ship diesel engine selected for the experiment.

2.2.2. Marine Fuel

Six kinds of marine fuels with different sulfur contents used in the experiment were 0.1%, 0.3%, 0.5%, 0.8%, 1.5%, 2.0%. They were representative of the sulfur content in actual marine fuels during navigation and berthing.

2.2.3. Working Condition of the Diesel Engine

When the same sulfur content is used in marine fuel, the different working conditions of the diesel engine yield a main effect on ship exhaust. The main diesel engine condition recorded in the experiment is shown in Table 1 as below.

Table 1. Main diesel engine condition recorded in the experiment.

Number	1	2	3	4	5	6	7	8	9	10	11	12	13
Power Percentage (%)	0	5	10	15	20	25	30	40	50	60	80	90	100

3. Results and Discussion

3.1. Bench Experiment Results

The bench test began at 9:53:05 on the first day and ended at 17:56:08 on the second day, during which 10,141 groups of gas concentration data were obtained. Figure 3 shows the changes in various gas concentrations.

3.2. Single-Wavelength Simulation Analysis Results

The RMSE, the MAE, and the MAPE in different detection wavelengths were arranged in order from small to large according to the single-wavelength simulation analysis data obtained from SAMID. Figure 6 shows the distribution of the top 10 errors. The RMSE, the MAE, and the MAPE all obtained minimum values when the wavelength was 287 nm. The minimum values of RMSE, MAE, and MAPE

were 563.14 molecules/cm³, 445.11 molecules/cm³, and 347.22%, respectively. Therefore, the optimal detection wavelength position of the single-wavelength detection technology was 287 nm. The error is so large that the single-wavelength detection technology is difficult when directly measuring the SO₂ concentration. In practical applications of the single-wavelength imaging detection technology, cells filled with different concentrations of SO₂ gas are required for calibration [12].

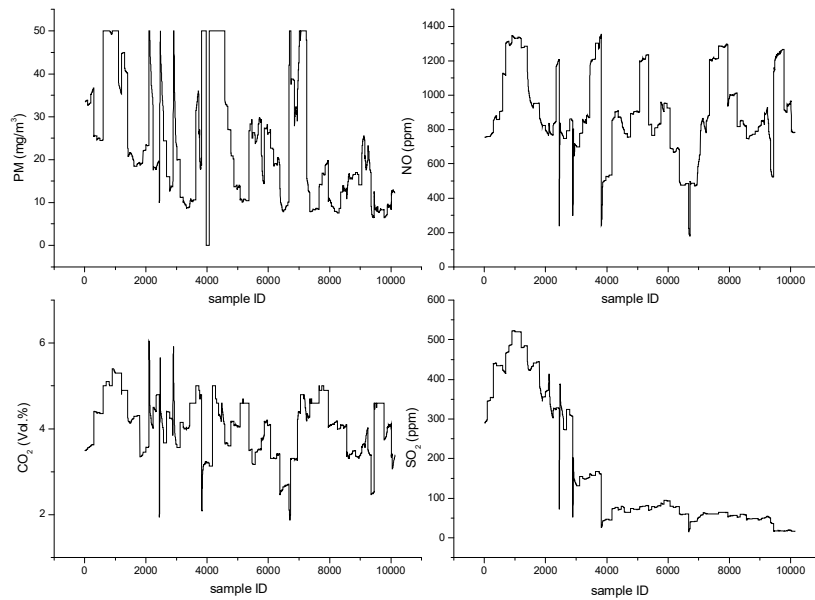


Figure 3. Changes in various gas concentrations.

The SO₂ emission is directly related to the sulfur content of fuel (Figure 4) [22,23], thereby providing a theoretical basis for calculating the sulfur content of fuel with the SO₂ concentration. The CO₂ emission depends on the engine load [24,25] and is not related to the fuel composition (Figure 5). Therefore, the sulfur–carbon ratio can be used to eliminate the influence of power and obtain a more accurate sulfur content of fuel.

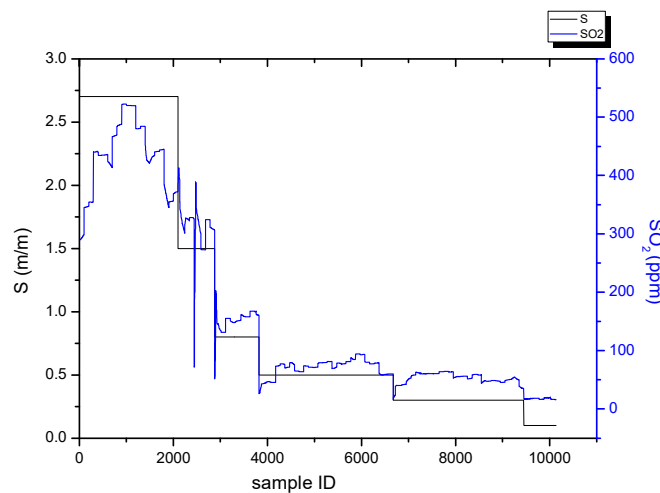


Figure 4. Changes in SO₂ concentration and sulfur content with time.

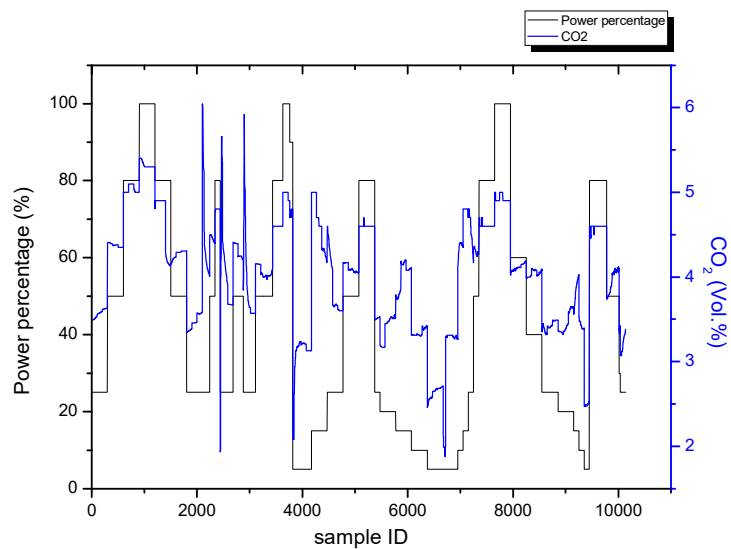


Figure 5. Changes in CO₂ concentration and engine load with time.

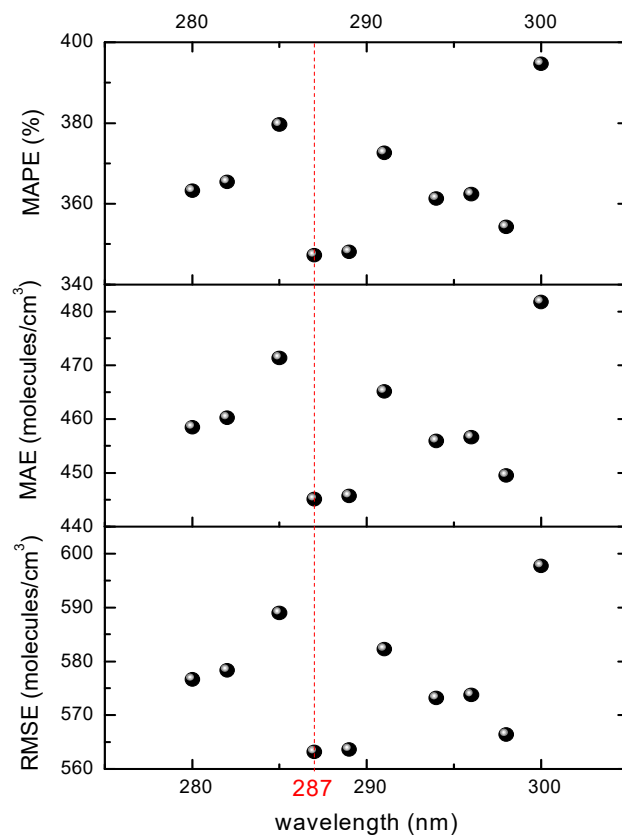


Figure 6. SO₂ single-wavelength error distribution. The red dot line indicates that the inversion using wavelength of 287 nm has the smallest error.

3.3. Dual-Wavelength Simulation Analysis Results

The minimum values of RMSE, MAE, and MAPE for each wavelength interval were taken according to the dual-wavelength simulation analysis data obtained from SAMID. Figure 7 shows the error variation with the wavelength interval. The optimal detection wavelength positions of the dual-wavelength detection technology were determined as 297 nm and 298 nm according to the principle of minimum error. The minimum values of RMSE, MAE, and MAPE were 0.62 molecules/cm³, 0.49 molecules/cm³, and 0.85%, respectively. The detection errors of the optimal detection wavelength

positions (i.e., 297 nm and 298 nm) were compared with those of the common volcano detection wavelength positions (i.e., 310 nm and 330 nm). Table 2 presents the relevant results.

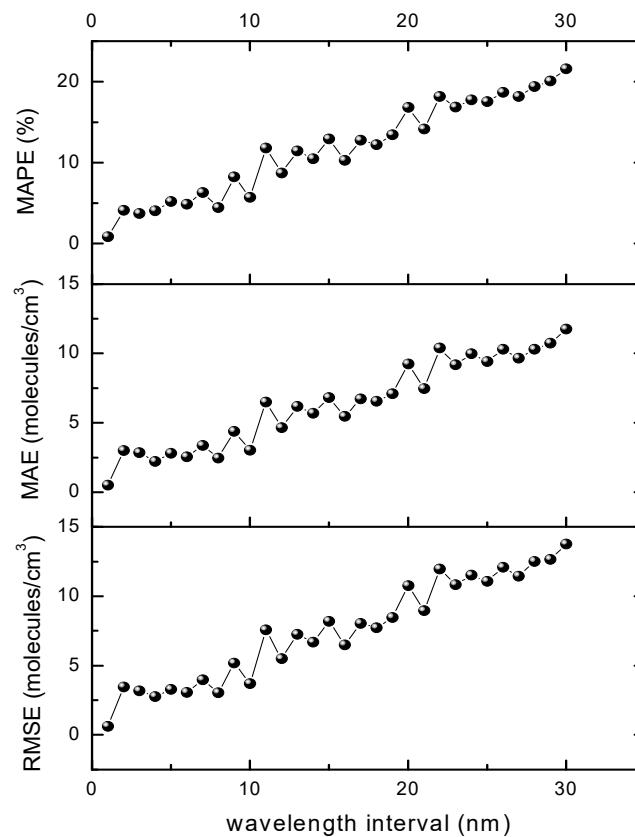


Figure 7. Variation of error with the wavelength interval.

Table 2. Comparison of the detection error between the optimal detection wavelength positions (i.e., 297 nm and 298 nm) and the common volcanic detection wavelength positions (i.e., 310 nm and 330 nm).

	RMSE (molecules/cm ³)	MAE (molecules/cm ³)	MAPE (%)
297 nm and 298 nm	0.62	0.49	0.85
310 nm and 330 nm	85.39	75.93	123.83

RMSE: root mean square error; MAE: mean absolute error; MAPE: mean absolute percentage error.

3.4. Calculation Results of the Sulfur Content

The formula for calculating the sulfur content of fuel is presented below considering the molecular weight of carbon (12 g/mol) and sulfur (32 g/mol) and the carbon mass percentage in fuel ($87 \pm 1.5\%$) [26]:

$$SFC[\%] \approx \frac{32 \times A(\text{SO}_2, \text{ppm})}{12 \times B(\text{CO}_2, \text{ppm}) / 0.87} \times 100 = 232 \times \frac{A(\text{SO}_2, \text{ppm})}{B(\text{CO}_2, \text{ppm})} = 0.0232 \times \frac{A(\text{SO}_2, \text{ppm})}{B(\text{CO}_2, \text{Vol.}\%)} \quad (16)$$

where $A(\text{SO}_2, \text{ppm})$ is the SO_2 concentration in ppm; $B(\text{CO}_2, \text{ppm})$ is the CO_2 concentration in ppm; $B(\text{CO}_2, \text{Vol.}\%)$ is the CO_2 concentration in Vol.%.

The SO_2 concentration obtained by the inversion at the optimal single-wavelength position (287 nm) was divided by the CO_2 concentration collected in the flue. The result was substituted into Equation (16) to obtain the predicted sulfur content. The SO_2 concentration obtained by the inversion of the optimal dual-wavelength positions at 297 nm and 298 nm was divided by the CO_2 concentration collected in the flue. Subsequently, the result was substituted into Equation (16) to obtain the sulfur

content predicted by the dual wavelength. The predicted values of each sulfur content were averaged and compared with the true sulfur content. Table 3 shows the results.

Table 3. Comparison between the average predicted and true sulfur contents.

True Sulfur Content	Sulfur Content (287 nm)	Error at 287 nm (%)	Sulfur Content (297 and 298 nm)	Error at 297 and 298 nm (%)
2.00	3.14	57.00	2.30	15.00
1.50	2.36	57.33	1.69	12.67
0.80	1.31	63.75	0.83	3.75
0.50	1.25	150.00	0.45	10.00
0.30	0.92	206.67	0.31	3.33
0.10	0.41	310.00	0.10	0.00

3.5. Discussion

Figure 6 indicates that the error of the single-wavelength imaging detection technology was too large for practical application. This is because the light diminution caused by other gases and particles is ignored in the single-wavelength imaging detection technology. However, the light diminution and enhancement along the path, which is caused by scattering and absorption within the band due to other gases and particles in realistic situations, can be quite complex and is difficult to model [27]. Thus, the single-wavelength imaging detection technology can only be used under ideal conditions, and equipment needs to be finely calibrated in practical applications. Meanwhile, Figure 7 depicts that the SO₂ concentration inversion results were relatively accurate, because the dual-wavelength detection technology can reduce the influence of NO₂ and BC extinction. The three errors of the dual-wavelength detection technology all tended to increase with the wavelength interval increase, because the larger the wavelength interval was, the greater the difference of NO₂ and BC extinction between the two wavelengths was, and less NO₂ and BC extinction was canceled out by the dual-wavelength difference.

As far as the simulation analysis results are concerned, Table 2 shows that the error obtained using the optimal detection wavelengths of 297 nm and 298 nm was much lower than that obtained using the common wavelengths of 310 nm and 330 nm for volcano detection. In other words, wavelength optimization has a certain guiding significance for improving the precision of the dual-wavelength imaging detection technology for ship exhaust.

As shown in Table 3, large errors can be found when calculating the sulfur content with the single-wavelength detection technology. Using the single-wavelength detection technology does not distinguish between different sulfur contents. The maximum error was only 15% after the predicted values of each sulfur content in the dual-wavelength were averaged. Apart from a few outliers, the dual-wavelength predicted value fluctuated around the true value in a sufficiently small range. Therefore, using the dual-wavelength detection technology can distinguish between different sulfur contents.

4. Conclusions

For the first time, this study established a simulation analysis model (i.e., SAMID model) of the optimal imaging detection wavelength of the SO₂ concentration in ship exhaust. The selection of the optimal detection wavelength position was studied through a simulation analysis. The simulation results showed that the optimal detection wavelength position of the single-wavelength was 287 nm, whereas that of the dual-wavelength was 297 nm and 298 nm. By comparing and analyzing the detection errors based on the single- and the dual-wavelength detection technologies, we conclude that the latter can largely remove the influence of NO₂ and BC extinction, obtain a more accurate SO₂ concentration, and improve the inversion accuracy. The predicted result of the sulfur content at the optimal dual wavelength (297 nm and 298 nm) was close to the true value, proving the feasibility of using the dual-wavelength imaging technology for the SO₂ concentration retrieval and calculating

the sulfur content of fuel. The research team will add more practical factors, such as filter bandwidth, on the basis of the current work to further improve the model, adjust the optimal detection wavelength position, and better guide the development of hardware equipment.

Author Contributions: Conceptualization, Z.Z. and W.Z.; methodology, Z.Z.; software, W.Z.; validation, Y.L., K.C. and M.X.; formal analysis, Z.Z.; investigation, K.C.; resources, Z.Z.; data curation, W.Z.; writing—original draft preparation, Z.Z.; writing—review and editing, Z.Z., W.Z., K.C., Y.L., M.X.; visualization, K.C.; supervision, Y.L.; project administration, Y.L.; funding acquisition, Y.L. All authors have read and agreed to the published version of the manuscript.

Funding: This study was supported financially by the National Key Research and Development Project (No. 2017YFC0211904), the Science and Technology Innovation Project of Dalian (No. 2018J11CY024) and the Fundamental Research Funds for the Central Universities (3132020130).

Acknowledgments: We gratefully acknowledge the valuable cooperation of Peng Wu and the members of his laboratory in preparing the data.

Conflicts of Interest: The authors declare no conflict of interest.

References

- Zhou, F.; Gu, J.; Chen, W.; Ni, X. Measurement of SO₂ and NO₂ in ship plumes using rotary unmanned aerial system. *Atmosphere* **2019**, *10*, 657. [CrossRef]
- IMO. Sulphur Oxides (SO_x) and Particulate Matter (PM)—Regulation 14. Available online: [http://www.imo.org/en/OurWork/Environment/PollutionPrevention/AirPollution/Pages/Sulphur-oxides-\(SOx\)-%E2%80%93-Regulation-14.aspx](http://www.imo.org/en/OurWork/Environment/PollutionPrevention/AirPollution/Pages/Sulphur-oxides-(SOx)-%E2%80%93-Regulation-14.aspx) (accessed on 26 October 2019).
- Sinha, P.; Hobbs, P.V.; Yokelson, R.J.; Christian, T.J.; Kirchstetter, T.W.; Bruintjes, R. Emissions of trace gases and particles from two ships in the southern Atlantic Ocean. *Atmos. Environ.* **2003**, *37*, 2139–2148. [CrossRef]
- Chen, G.; Huey, L.G.; Trainer, M.; Nicks, D.; Corbett, J.; Ryerson, T.; Ryerson, T.; Parrish, D.; Neuman, J.A.; Nowak, J.M.; et al. An investigation of the chemistry of ship emission plumes during ITCT 2002. *J. Geophys. Res. Atmos.* **2005**, *110*. [CrossRef]
- Mellqvist, J.; Berg, N.; Ohlsson, D. Remote surveillance of the sulfur content and NO_x emissions of ships. In Proceedings of the 2nd International Conference on Harbor, Air Quality and Climate Changes (HAQCC), Rotterdam, The Netherlands, 29–30 May 2008.
- Alfoeldy, B.; Loeoev, J.B.; Lagler, F.; Mellqvist, J.; Berg, N.; Beecken, J.; Weststrate, H.; Duyzer, J.; Bencs, L.; Horemans, B.; et al. Measurements of air pollution emission factors for marine transportation in SECA. *Atmos. Meas. Tech.* **2013**, *6*, 1777–1791. [CrossRef]
- Beecken, J.; Mellqvist, J.; Salo, K.; Ekholm, J.; Jalkanen, J.-P. Airborne emission measurements of SO₂, NO_x and particles from individual ships using sniffer technique. *Atmos. Meas. Tech.* **2013**, *7*, 1957–1968. [CrossRef]
- Loov, J.M.B.; Alföldy, B.; Gast, L.F.L.; Hjorth, J.; Lagler, F.; Mellqvist, J.; Beecken, J.; Berg, N.; Duyzer, J.; Weststrate, H.; et al. Field test of available methods to measure remotely SO_x and NO_x emissions from ships. *Atmos. Meas. Tech.* **2014**, *7*, 2597–2613. [CrossRef]
- Volten, H.; Brinksma, E.J.; Berkhout, A.J.C.; Hains, J.; Bergwerff, J.B.; Van der Hoff, G.R.; Apituley, A.; Dirksen, R.J.; Calabretta-Jongen, S.; Swart, D.P.J. NO₂ lidar profile measurements for satellite interpretation and validation. *J. Geophys. Res. Atmos.* **2009**, *114*. [CrossRef]
- Platt, U.; Perner, D.; Pätz, H.W. Simultaneous measurement of atmospheric CH₂O, O₃, and NO₂ by differential optical absorption. *J. Geophys. Res.* **1979**, *84*, 6329–6335. [CrossRef]
- Merico, E.; Donato, A.; Gambaro, A.; Cesari, D.; Gregoris, E.; Barbaro, E.; Dinoi, A.; Giovanelli, G.; Masieri, S.; Contini, D. Influence of in-port ships emissions to gaseous atmospheric pollutants and to particulate matter of different sizes in a Mediterranean harbor in Italy. *Atmos. Environ.* **2016**, *139*, 1–10. [CrossRef]
- Prata, A.J. Measuring SO₂ ship emissions with an ultraviolet imaging camera. *Atmos. Meas. Tech.* **2014**, *7*, 1213–1229. [CrossRef]
- Campion, R.; Martinez-Cruz, M.; Lecocq, T.; Caudron, C.; Pacheco, J.; Pinardi, G.; Hermans, C.; Carn, S.; Bernard, A. Space-and ground-based measurements of sulphur dioxide emissions from Turrialba Volcano (Costa Rica). *Bull. Volcanol.* **2012**, *74*, 1757–1770. [CrossRef]

14. Kern, C.; Kick, F.; Luebeck, P.; Vogel, L.; Woehrbach, M.; Platt, U. Theoretical description of functionality, applications, and limitations of SO₂ cameras for the remote sensing of volcanic plumes. *Atmos. Meas. Tech.* **2010**, *3*, 733–749. [[CrossRef](#)]
15. Kantzas, E.P.; McGonigle, A.J.S.; Tamburello, G.; Aiuppa, A.; Bryant, R.G. Protocols for UV camera volcanic SO₂ measurements. *J. Volcanol. Geother. Res.* **2010**, *194*, 55–60. [[CrossRef](#)]
16. Champion, R.; Delgado-Granados, H.; Legrand, D.; Taquet, N.; Boulesteix, T.; Pedraza-Espitia, S.; Lecocq, T. Breathing and coughing: The extraordinarily high degassing of Popocatepetl volcano investigated with an SO₂ camera. *Front. Earth Sci.* **2018**, *6*, 163. [[CrossRef](#)]
17. Buffaloe, G.M.; Lack, D.A.; Williams, E.J.; Coffman, D.; Hayden, K.L.; Lerner, B.M.; Li, S.M.; Nuaaman, I.; Massoli, P.; Onasch, T.B.; et al. Black carbon emissions from in-use ships: A California regional assessment. *Atmos. Chem. Phys.* **2014**, *14*, 1881–1896. [[CrossRef](#)]
18. Reilly, D.M.; Moriarty, D.T.; Maynard, J.A. Unique properties of solar blind ultraviolet communication systems for unattended ground sensor networks. In Proceedings of the SPIE—The International Society for Optical Engineering, Beijing, China, 8 November 2004; pp. 244–254.
19. Johan, R.; Conde, V.; Beecken, J.; Ekholm, J. *Certification of An Aircraft and Airborne Surveillance of Fuel Sulfur Content in Ships at the SECA Border*; Department of Earth and Space Sciences, Chalmers University of Technology: Göteborg, Sweden, 2017.
20. Luebecke, P.; Bobrowski, N.; Illing, S.; Kern, C.; Nieves, J.M.A.; Vogel, L.; Zielcke, J.; Granados, H.D.; Platt, U. On the absolute calibration of SO₂ cameras. *Atmos. Measur. Tech.* **2013**, *6*, 6183–6420. [[CrossRef](#)]
21. Gordon, I.E.; Rothman, L.S.; Hill, C.; Kochanov, R.V.; Tan, Y.; Bernath, P.F.; Birk, M.; Boudon, V.; Campargue, A.; Chance, K.V.; et al. The HITRAN 2016 molecular spectroscopic database. *J. Quant. Spectrosc. Radiat. Trans.* **2017**, *203*, 3–69. [[CrossRef](#)]
22. Cooper, D.; Gustafsson, T. *Methodology for Calculating Emissions from Ships: 1. Update of Emission Factors; Swedish Methodology for Environmental Data*: Uppsala, Sweden, 2004.
23. Smith, T.; Jalkanen, J.P.; Anderson, B.A.; Corbett, J.J.; Pandey. *Third IMO GHG Study 2014: Executive Summary and Final Report*; International Maritime Organization (IMO): London, UK, 2014.
24. Winnes, H.; Fridell, E. Emissions of NO_x and particles from manoeuvring ships. *Transp. Res. Part D Trans. Environ.* **2010**, *15*, 204–211. [[CrossRef](#)]
25. Winnes, H.; Fridell, E. Particle emissions from ships: Dependence on fuel type. *J. Air Waste Manag. Assoc.* **2009**, *59*, 1391–1398. [[CrossRef](#)]
26. Cooper, D.A. HCB, PCB, PCDD and PCDF emissions from ships. *Atmos. Environ.* **2005**, *39*, 4901–4912. [[CrossRef](#)]
27. Kern, C.; Deutschmann, T.; Vogel, L.; Wöhrbach, M.; Wagner, T.; Platt, U. Radiative transfer corrections for accurate spectroscopic measurements of volcanic gas emissions. *Bull. Volcanol.* **2013**, *72*, 233–247. [[CrossRef](#)]

Publisher’s Note: MDPI stays neutral with regard to jurisdictional claims in published maps and institutional affiliations.



© 2020 by the authors. Licensee MDPI, Basel, Switzerland. This article is an open access article distributed under the terms and conditions of the Creative Commons Attribution (CC BY) license (<http://creativecommons.org/licenses/by/4.0/>).